
Fast Inference Using Automatic Differentiation and Neural Transport in Astroparticle Physics

Dorian W. P. Amaral* 

Department of Physics and Astronomy
Rice University
Houston, TX, 77005, U.S.A.
dorian.amaral@rice.edu

Shixiao Liang* 

Department of Physics and Astronomy
Rice University
Houston, TX, 77005, U.S.A.
liangsx@rice.edu

Juehang Qin* 

Department of Physics and Astronomy
Rice University
Houston, TX, 77005, U.S.A.
qinjuehang@rice.edu

Christopher Tunnell 

Department of Physics and Astronomy
Department of Computer Science
Rice University
Houston, TX, 77005, U.S.A.
tunnell@rice.edu

Abstract

Multi-dimensional parameter spaces are commonly encountered in astroparticle physics theories that attempt to capture novel phenomena. However, they often possess complicated posterior geometries that are expensive to traverse using techniques traditional to this community. Effectively sampling these spaces is crucial to bridge the gap between experiment and theory. Several recent innovations, which are only beginning to make their way into this field, have made navigating such complex posteriors possible. These include GPU acceleration, automatic differentiation, and neural-network-guided reparameterization. We apply these advancements to astroparticle physics experimental results in the context of novel neutrino physics and benchmark their performances against traditional nested sampling techniques. Compared to nested sampling alone, we find that these techniques increase performance for both nested sampling and Hamiltonian Monte Carlo, accelerating inference by factors of ~ 100 and ~ 60 , respectively. As nested sampling also evaluates the Bayesian evidence, these advancements can be exploited to improve model comparison performance while retaining compatibility with existing implementations that are widely used in the natural sciences.

1 Introduction

The Standard Model of particle physics, our best description of the fundamental building blocks of the Universe, is an incomplete description of nature. To better capture reality, theories that go beyond the Standard Model are needed [1–3]. These theories often feature multi-dimensional parameter spaces (with order 10 parameters or more) that must be explored to determine regions that are allowed by the observed data [4–9]. However, methods for doing so that are traditional to the physics community, such as nested sampling (NS), often slow down when navigating complicated posterior geometries [10–13]. This problem is particularly acute in the *limit-setting* regime, where no significant novel signal is observed and the data is used to restrict the domain of the theory. In this regime, the likelihood is often diffuse and lacks strong modes, rendering it difficult to explore.

*Equal contribution.

The problem is exacerbated when the likelihood is expensive to evaluate, as is often true due to the complexity of theoretical frameworks. These issues make it challenging to diagnose convergence failures, incorporate new experimental data, and produce timely studies.

These problems can be tackled using a combination of methods. Leveraging recent powerful numerical computing frameworks, such as JAX [14], and probabilistic programming frameworks, such as `numpyro` [15, 16], allows us to automatically differentiate likelihood functions and thus sample efficiently using Hamiltonian Monte Carlo (HMC) [17, 18] and the No-U-Turn Sampler (NUTS) [19]. For likelihood functions that are computationally expensive but vectorizable, GPU acceleration can also confer a significant performance boost. Finally, normalizing flows can be used as a reversible transformation to obtain a posterior distribution that is easier to explore in a technique known as neural transport (NeuTra) [20].

In this work, we study the use of GPU acceleration, differentiable likelihoods, and NeuTra in the context of neutrino astroparticle physics. We begin by studying the performance boosts that can be achievable using differentiable likelihoods and NeuTra with a synthetic problem based on a multi-dimensional Gaussian fit. We then apply these methods and GPU acceleration within the context of *neutrino non-standard interactions* (NSI) [9, 21–28]: a multi-dimensional parameterization describing novel phenomena with neutrinos. We perform statistical inference within this framework using results from the astroparticle experiments XENON1T [29] and PandaX-4T [30]. We provide our code in [🔗](#).

2 Background

2.1 Sampling Methods

Nested sampling Nested sampling is a family of Monte Carlo methods for calculating integrals over a parameter space [31, 32]. It can also be used for Bayesian computation and has gained popularity for its success in multi-modal problems and its self-tuning feature [33]. NS has many applications in various fields, such as biology [34, 35], linguistics [36, 37] and the physical sciences [38]—including particle physics [39, 40].

Consider a parameter space θ for which we wish to compute the posterior distribution $p(\theta|\mathbf{X})$, where \mathbf{X} represents the experimental data. NS works by iteratively sampling live points from the prior distribution, $\pi(\theta)$, commencing by sampling N live points within its support. Following this, the live point with the lowest likelihood value, L_1 , is removed, and a new live point is sampled from the restricted parameter space, where the likelihood for the parameters in this space must be higher. This process continues, with sampling taking place within the contour defined by the live point with the lowest likelihood in the i^{th} iteration, L_i . Concretely, the distribution being sampled from in the i^{th} iteration is

$$p_i(\theta) \propto \begin{cases} \pi(\theta) & \text{if } p(\mathbf{X}|\theta) > L_i \\ 0 & \text{if } p(\mathbf{X}|\theta) \leq L_i \end{cases}, \quad (1)$$

where $p(\mathbf{X}|\theta)$ is the likelihood of the data \mathbf{X} given the parameters θ . Increasing the likelihood threshold reduces the volume of the likelihood-restricted parameter space by a factor that obeys a Beta(1, N) distribution. This factor is approximately given by $\Delta V_i = V_i/N$, where V_i is the volume of the likelihood-restricted parameter space in the i^{th} iteration.

Nested sampling stops when a predetermined halting criterion is met. One example of such a criterion is to require that the removed points represent a certain fraction of the total Bayesian evidence integral. The Bayesian evidence, \mathcal{Z} , can be estimated using the removed points and the remaining live points at termination via

$$\mathcal{Z} \equiv \int p(\theta|\mathbf{X}) d\theta \simeq \sum_{i=1}^{N_{\text{iter}}} \Delta V_i L_i + \frac{V_{\text{end}}}{N} \sum_{j=1}^N L_j, \quad (2)$$

where the sum over j represents a sum over the likelihoods of the remaining live points at termination, N_{iter} is the total number of iterations, and V_{end} is the remaining volume at termination. The posterior distribution can then be inferred using the removed points and the remaining live points at termination weighted by $\Delta V_i L_i$ and V_{end}/N , respectively. The ability to provide both the evidence and the posterior distribution makes NS a powerful method for Bayesian computation.

HMC/NUTS Hamiltonian Monte Carlo is a powerful sampling algorithm that leverages gradient information to efficiently explore complex probability distributions [17, 18, 41]. HMC offers improved performance compared to traditional Markov chain Monte Carlo (MCMC) methods using a simulation of Hamiltonian dynamics to explore a target parameter space more efficiently than random walks. However, The effectiveness of HMC relies on careful tuning. The NUTS sampler with dual-averaging alleviates this need by adaptively adjusting HMC parameters [42, 43], and it has been widely adopted and implemented across various probabilistic programming frameworks [15, 16, 19, 44, 45].

HMC is extensively used across both the natural and social sciences, and it has been recently employed for analyzing neutrino experiment results [17, 46–50]. Because HMC is a gradient-based sampling method, it requires the model to either support automatic differentiation or have known derivatives. Interest in it has thus led to new implementations of models using frameworks compatible with automatic differentiation [51, 52].

Neural Transport While NS and HMC are better at exploring complex posteriors than simpler methods, such as basic rejection sampling with uniform proposals, sampling efficiency still drops for sufficiently challenging posteriors in multiple dimensions [32, 53]. Under these circumstances, reparameterization can improve the performance of inference algorithms [54], which can be non-trivial for likelihoods that cannot be easily expressed as hierarchical Bayesian models.

One way to remedy this is to use a reversible transformation to map a posterior distribution onto one that is easier to sample, such as a standard normal distribution [20]. Instead of directly sampling from the posterior $p(\theta|\mathbf{X})$ using HMC or NS, we can consider a bijective function \mathbf{f} that defines the reparameterization of our distribution. This function acts on the reparameterized latent space \mathbf{z} , such that $\theta = \mathbf{f}(\mathbf{z})$. We can then instead sample from the distribution

$$p(\mathbf{z}) \equiv p(\theta = \mathbf{f}(\mathbf{z})|\mathbf{X}) \left| \frac{\partial \mathbf{f}}{\partial \mathbf{z}} \right|, \quad (3)$$

where $|\partial \mathbf{f} / \partial \mathbf{z}|$ is the determinant of the Jacobian of the parameter transformation. Eq. (3) generally follows from the reparameterization of probability distributions, as shown in Appendix A.

Subsequently, the pushforward $\mathbf{f}(\mathbf{z})$ can be used to obtain the desired samples of $p(\theta|\mathbf{X})$. Normalizing flows are a good candidate to parameterize the bijective function, as they can be highly expressive and can be fit by minimizing the Kullback–Leibler (KL) divergence. Using them to reparameterize Bayesian models is known as Neural Transport (NeuTra), as introduced in [20]. There, NeuTra with inverse autoregressive flows was shown to improve sampling performance in problems with difficult posterior distributions. Instead of inverse autoregressive flows, we use block neural autoregressive flows, which demonstrate improved performance over earlier methods [55].

To train a normalizing flow that can transform the posterior distribution of interest into a standard normal distribution, we maximize the evidence lower bound (ELBO) [20, 56], which is equivalent to minimizing the KL divergence [57]. Given $\mathbf{f}_\phi(\mathbf{z})$ —the transformation represented by a normalizing flow with parameters ϕ —the distribution over θ is

$$q_\phi(\theta) \equiv q_\phi(\mathbf{z}) \left| \frac{\partial \mathbf{f}}{\partial \mathbf{z}} \right|^{-1}, \quad (4)$$

where $q_\phi(\mathbf{z})$ is the target distribution in the transformed space, which is a standard normal distribution in our case. The ELBO can then be written as

$$\mathcal{L}(\phi) = \mathbb{E}_{q_\phi(\mathbf{z})} \left[\log(p(\mathbf{X}, \mathbf{f}_\phi(\mathbf{z}))) - \log \left(q_\phi(\mathbf{z}) \left| \frac{\partial \mathbf{f}}{\partial \mathbf{z}} \right|^{-1} \right) \right], \quad (5)$$

and we can thus estimate it using a set of samples from a standard normal distribution.

2.2 Neutrinos, Astroparticle Experiments, and Novel Physics

Neutrinos at Astroparticle Experiments Neutrinos are fundamental particles created by the radioactive decay of unstable atomic nuclei. This occurs in places like nuclear reactors, atomic bombs, and the Sun. Neutrinos come in three *flavors*—electron (e), muon (μ), and tau (τ)—and quantum

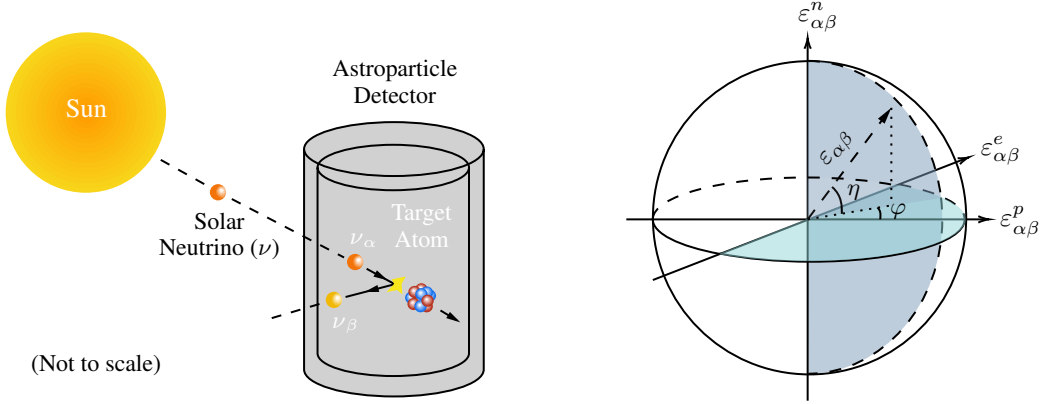


Figure 1: **Left:** Experimental idea. Solar neutrinos collide with the target atoms in an astroparticle detector, which can be thought of as a $\sim 1 \text{ m}^3$ tank of liquid xenon. These collisions cause either the nucleus or the electrons of the atom to recoil, which we observe. We have exaggerated the size of the target atom and neutrinos. **Right:** The neutrino non-standard interactions parameterization, which can be used to model new physics phenomena between neutrinos, neutrons (n), protons (p), and electrons (e) [9]. It is characterized by an overall interaction strength coordinate, $\varepsilon_{\alpha\beta}$, and two angles describing how strong the interaction is with the neutron (η) and proton vs. electron (φ).

mechanical effects lead to them oscillating between these flavors [58, 59]. This transmutation is one of the best pieces of evidence we have for physics beyond the Standard Model, making them excellent candidates with which to search for novel phenomena [60]. Experiments sensitive to neutrino interactions can thus probe phenomena beyond the Standard Model.

Among these experiments are *direct detection* experiments. Originally leading the hunt for dark matter, these astroparticle detectors are beginning to have exquisite sensitivity to neutrinos produced in the Sun [61]. Two such experiments are XENON1T [62] and PandaX-4T [63]. Solar neutrinos travel to these detectors, interact with the material, and cause the recoil of either a target nucleus or electron. We illustrate this in Fig. 1 (left). We can count the number of nuclear recoils (NRs) and/or electron recoils (ERs) and use it to answer the question of whether or not it is consistent with the prediction from the Standard Model of particle physics.

Neutrino Non-Standard Interactions Neutrino physics that goes beyond the Standard Model can be described using the framework of neutrino non-standard interactions [21–27]. In this framework, we can make predictions by sampling from an 8-dimensional parameter space defined by the coordinates $(\varepsilon_{\alpha\beta}, \eta, \varphi)$ [9]. Here, the 6 parameters $\varepsilon_{\alpha\beta}$ characterize the overall strength and type of interaction. There is one such parameter for each flavor combination $\alpha\beta$ ($ee, e\mu, e\tau$, etc.), with equal flavor indices meaning that the neutrino type remains the same after the interaction and unequal indices indicating that it changes. The remaining two parameters (η, φ) are angles describing how strongly the new interaction takes place with protons, neutrons, and electrons. The angle η models how strongly the interaction is with the neutron, and the angle φ characterizes the strength of the interaction between the electrically charged proton and electron. We visualize the NSI parametrization in Fig. 1 (right) and further discuss it in Appendix B.

Within this framework, we calculate the number of expected NRs and ERs using the SNUDD Python package [9, 64]. Given a choice of NSI parameters, it computes the number of recoils

$$N_{\text{NR/ER}} = \iint \text{SNUDD}(\varepsilon_{\alpha\beta}, \eta, \varphi; E_\nu, E_R) dE_\nu dE_R, \quad (6)$$

where the integrand is a function encapsulating the physics of the problem. The integrals are over all the possible solar neutrino energies, E_ν , and measurable recoil energies, E_R . The presence of this double integral makes Eq. (6) a prime candidate for GPU acceleration.

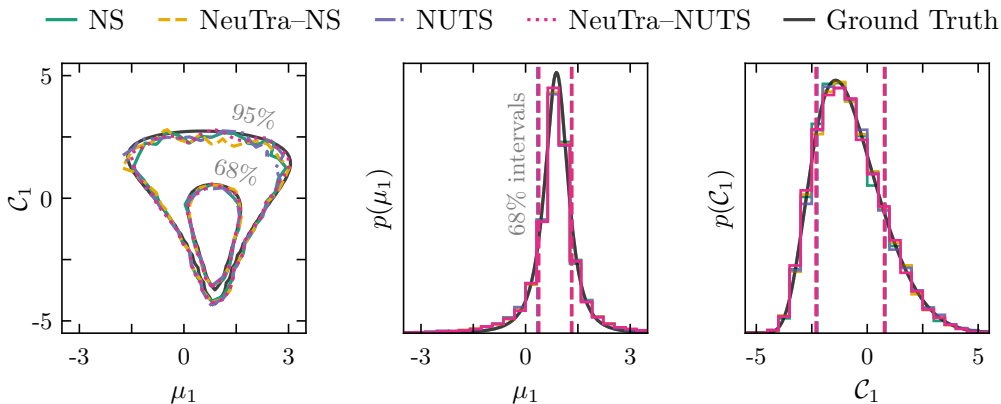


Figure 2: Marginalized representations of the inferred posteriors for our synthetic model, Eq. (7), using nested sampling (NS) and the No U-Turn Sampler (NUTS), both with and without neural transport (NeuTra). **Left:** The 68% and 95% highest posterior density region contours. **Middle and Right:** Probability density of the samples with 68% equal-tailed intervals indicated as dashed lines. Only μ_1 and C_1 are shown for clarity; the full corner plot is given in Appendix E. As desired, our results show a high degree of overlap and all closely match the ground truth, derived in Appendix C.

3 Experiments

3.1 Gaussian Fit with Unknown Mean and Variance

Before applying our sampling methods to the neutrino physics problem, we compare them using a simpler synthetic problem. This is based on a Gaussian fit with unknown mean and standard deviation with a centered parameterization. This is chosen to demonstrate the performance of the various methods using a model that is known to be difficult to sample without reparameterization [54]. The likelihood has a similar structure to the well-known Neal’s funnel [65]; however, this was chosen as a more difficult problem, as Neal’s funnel was efficiently handled by nested sampling as implemented in *ultranest* [66]. Our model is given by

$$\mu_i \sim \mathcal{N}(0, 10), \quad C_i \sim \mathcal{N}(0, 10), \quad x_{ij} \sim \mathcal{N}(\mu_i, e^{C_i}), \quad (7)$$

where μ_i are means, C_i are log variances, and x_{ij} are the observed variables. For our experiments, we fit 3-dimensional data generated from a standard normal distribution, and the observed dataset has 2 data points, such that $i \in \{1, 2, 3\}$ and $j \in \{1, 2\}$.

We sample from this model using NS and NUTS, both with and without NeuTra. For NS, the number of live points is 1600 without neural transport and 2400 with neural transport, as this is found to produce 1.4×10^4 effective samples in both cases. We use a sigmoid to transform the parameter space into the unit cube for NS runs. The log-determinant of the transformation Jacobian is summed into the log-density to ensure that the posterior is unaltered by this procedure. For NUTS, each of the 4 chains we use has a length of 3000 warmup steps and 5000 samples with a target acceptance probability of 0.8. We implement NeuTra with Block Neural Autoregressive Flows [55] using two flows with hidden dimensions [4, 4]. We train the NeuTra model on the ELBO estimated using 30 points for 5000 epochs. We run all experiments on an Intel Xeon Gold 6230 CPU. The ground truth evidence and contour integrals are analytically evaluated where possible, and we use *torchquad* [67] to compute the remaining integrals via non-stochastic numerical integration; we describe this procedure in greater detail in Appendix C.

Results To compare the performance of NUTS and NS, both with and without NeuTra, we use the metrics of wall time per effective sample size (ESS), and likelihood or gradient evaluation per ESS. For NUTS, as ESS can be different for each parameter, the minimum ESS is used, following [19]. The calculation of ESS for MCMC and NS is explained in Appendix D. We note that the ESS per evaluation metric is not directly comparable between NS and NUTS because gradient evaluations are required for NUTS and not for NS. We also include the number of divergences encountered per

Method	Wall Time per ESS [ms]	Eval. per ESS	Div. per ESS [$\times 10^{-2}$]
NS	16.0 ± 0.1	20.8 ± 0.4	N/A
NeuTra–NS	12.0 ± 0.6	10 ± 1	N/A
NUTS	4.8 ± 0.3	86 ± 6	3 ± 2
NeuTra–NUTS	1.4 ± 0.2	9.6 ± 0.5	0

Table 1: Synthetic model performance of our sampling methods: nested sampling (NS) and the No U-Turn Sampler (NUTS), both with and without neural transport (NeuTra). Reported are the wall time per effective sample size (ESS), the number of gradient or likelihood (in the case of NS) evaluations per ESS, and the number of divergences normalized by the ESS. NS is run 4 times with and without NeuTra to estimate the 1σ errorbars of performance indicators, whereas with NUTS they are computed using the chain-to-chain variation.

ESS for NUTS runs, as these indicate regions of high curvature that often cannot be reliably sampled by MCMC [41].

We show the marginalized posteriors for μ_1 and C_1 in Fig. 2, produced using corner [68]. We see that the 68% and 95% highest posterior density region contours, as well as the probability densities of these parameters, all show a high degree of overlap. Our results also agree with the ground truth. The full corner plot for all parameters is shown in Appendix E, and they exhibit the same behaviors.

Our numerical results are summarised in Table 1. For the evaluation per ESS, we see that NeuTra improves the performance of NS by a factor of ~ 2 and that of NUTS by a factor of ~ 9 . The improvements in wall time are smaller; this is because the normalizing flow used for NeuTra has non-zero evaluation time. However, we expect the improvement in wall time and the number of likelihood function evaluations to converge for real-life problems with computationally expensive likelihood functions. Our results thus indicate that for problems with cheap likelihood functions, NeuTra–NUTS yields the best performance.

We also find that the evidence computed using nested sampling, shown in Appendix F, matches the ground truth value of -11.14 . The mean ELBO from the last 100 epochs of neural transport training, -11.21 , is also close to the ground truth value. This demonstrates that NeuTra can be applied to NS to accelerate Bayesian evidence computation and model comparison.

3.2 Application to Neutrino Physics

Neutrino Physics Model For our physics application, we construct our likelihood using the NR result from XENON1T [29] and the ER measurement from PandaX-4T [30]. These measurements probe complementary parts of the NSI parameter space, allowing us to make stronger inferences compared to using either result alone.

For the XENON1T NR measurement, the data contains both solar neutrino events and background events that are unrelated to our signal of interest. As our likelihood model, we use a Poisson distribution with expectation value $\lambda \equiv \lambda_{\text{NR}} + \lambda_{\text{bkg}}$. Here, λ_{NR} is the expected number of NR events, calculated using SNUDD via Eq. (6), and λ_{bkg} is the expected number of background events. As given in [29], we use $\lambda_{\text{bkg}} = 5.38$ and take the number of observed NR events to be $N_{\text{NR}} = 6$.

For the PandaX-4T ER result, we use their inferred result on the number of solar neutrinos arriving at the detector per second per unit area, which is proportional to the number of ER events. As in the NR case, we use SNUDD to compute the number of expected ER events for a given set of NSI parameters. We then compare this number to the one calculated in the absence of novel phenomena using the ratio between the two values, r_{ER} . We model the distribution of this ratio as a normal distribution truncated at zero at the lower end with mean and standard deviation both given by 1.72. The truncation is to indicate that this physical quantity is strictly positive. The value 1.72 is calculated according to the mean and uncertainty reported in [30]. The above procedure gives rise to an additional likelihood term that can be used to make inferences on the number of ER events.

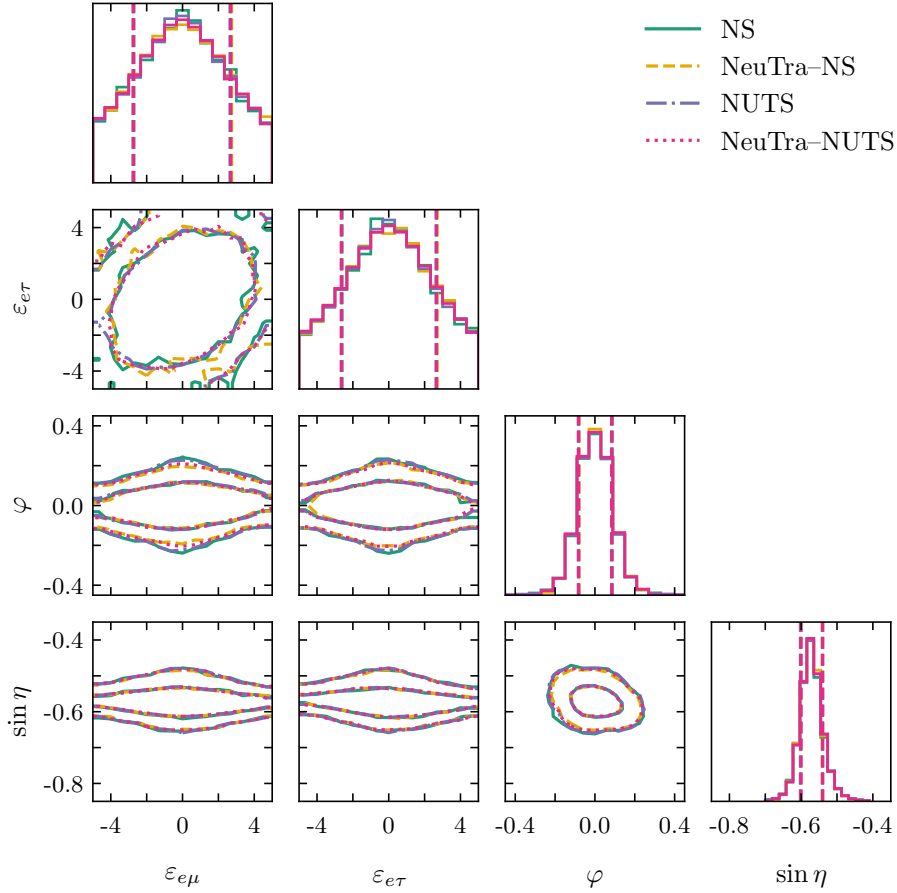


Figure 3: The 68% and 95% contours for the inferred posteriors for the neutrino non-standard interactions parameters. Our sampling methods are nested sampling (NS) and the No U-Turn Sampler (NUTS), both with and without neural transport (NeuTra). Two of the six $\varepsilon_{\alpha\beta}$ are selected to be shown for visualization purposes; the full corner plot is given in Appendix E. As desired, all contours show a high degree of overlap. Probability densities are also shown with 68% equal-tailed intervals indicated as dashed lines. The intervals from all methods are almost identical.

For the NSI parameters, we take $\varepsilon_{\alpha\beta}$ to be uniformly distributed over the range $(-5, 5)$. Moreover, we take φ to be uniformly distributed over the range $(-\pi/2, \pi/2)$. Lastly, to ensure even sampling on the iso- $\varepsilon_{\alpha\beta}$ sphere, we set the prior on $\sin \eta$ to be distributed uniformly over $(-1, 1)$. We physically motivate these priors in Appendix B. The full model is summarized below:

$$\begin{aligned} \varepsilon_{\alpha\beta} &\sim \text{Uniform}(-5, 5), \quad \varphi \sim \text{Uniform}(-\pi/2, \pi/2), \quad \sin \eta \sim \text{Uniform}(-1, 1), \\ N_{\text{NR}} &\sim \text{Poisson}(\lambda_{\text{bkg}} + \lambda_{\text{NR}}(\varepsilon_{\alpha\beta}, \eta, \varphi)), \quad r_{\text{ER}} \sim \text{TruncatedNormal}(1.72, 1.72^2, 0, \infty). \end{aligned} \quad (8)$$

We evaluate 10^4 likelihoods with the NSI parameters randomly sampled from the priors given in Eq. (8). We perform these calculations using both an Intel Xeon Gold 6230 CPU and an Nvidia Titan V GPU. As in Section 3.1, we implement NeuTra with Block Neural Autoregressive Flows, this time using three flows with hidden dimensions $[10, 10]$. The NeuTra model is trained on ELBO estimated using 30 points for 10^4 epochs.

For the NS runs, we use 1200 live points without NeuTra and 800 live points with NeuTra to produce similar ESSs of approximately 4200. NS runs are halted when the area of the Bayesian evidence integral covered by the remaining live points drops below 2%; this was increased from the `ultranest` default of 1% due to computational expense. We separately run NS with GPU disabled to compare the performance. This run has a smaller ESS of ~ 800 due to computational constraints; this causes

Method	Wall Time per ESS [s]	Eval. per ESS	Div. per ESS [$\times 10^{-4}$]
NS (CPU, scaled)	130 ± 20	1500 ± 300	N/A
NS (GPU)	9 ± 3	1500 ± 600	N/A
NeuTra–NS	0.9 ± 0.1	150 ± 20	N/A
NUTS	5.6 ± 0.2	195 ± 7	11 ± 5
NeuTra–NUTS	2.2 ± 0.2	80 ± 7	2.3 ± 0.9

Table 2: Neutrino non-standard interaction model performance of our sampling methods: nested sampling (NS) and the No U-Turn Sampler (NUTS), both with and without neural transport (NeuTra). Reported are the effective sample size (ESS) per wall time, the gradient or likelihood (in the case of NS) evaluation per ESS, and the number of divergences normalized by the ESS. The wall time and number of evaluations per ESS are scaled by a factor of 2.4 so that the evaluations per ESS are consistent between CPU and GPU runs. NS is run 6 times with and without NeuTra to estimate the 1σ errorbars of performance indicators, whereas with NUTS they are computed using the chain-to-chain variation.

the ESS per evaluation to be higher. When calculating improvement factors, we therefore multiply the wall time per ESS of the CPU NS run by 2.4 to match the likelihood function evaluation per ESS with that of the GPU run.

For the NUTS runs, we generate 10^5 samples both with and without NeuTra. We find that manually setting the step length parameter reduces the number of divergences encountered, and thus set the step size to 0.12 and 0.06 for NUTS with and without NeuTra, respectively. The samples are generated over 20 chains, with 2000 warm-up steps and 5000 sampling steps each.

Results We compare the performance of NS and NUTS, both with and without NeuTra, using the same metrics as in Section 3.1. In addition, we assess the GPU acceleration by comparing the time taken for a single likelihood evaluation. When the GPU is enabled, we find that one such evaluation takes 3.84 ± 0.01 ms compared to 67 ± 4 ms when it is disabled. Using the GPU therefore results in a speedup of ~ 20 times compared to running on the CPU.

We show the marginalized posteriors for a subset of the NSI parameters in Fig. 3, produced using corner [68]. As in Section 3.1, the 68% and 95% highest posterior density region contours, as well as the probability densities, all agree. Due to the complexity of the model, no ground truth contour is derived. The full corner plot for all NSI parameters is shown in Appendix E and all demonstrate the same level of agreement.

We summarize our performances in Table 2. For the NUTS sampler, we compute the ESS separately for each dimension. We use the minimum ESS across all dimensions, which is either φ or $\sin \eta$, to characterize the performance following [19]. We find that employing NeuTra to NUTS improves the efficiency by a factor of 2 and reduces the number of divergences by a factor of 5. Applying NeuTra to NS accelerates it by a larger factor of 10. We therefore find that NeuTra–NS provides the greatest performance in the NSI problem.

Unlike for our synthetic problem where NeuTra–NUTS was more performant, NeuTra–NS is the better choice for our physics problem. We believe that this is due to the computational expense of gradient evaluations given the complexity of our likelihood function. This highlights how the optimal strategy for sampling statistical problems needs to be evaluated on a case-by-case basis.

Nevertheless, as with the synthetic problem in Section 3.1, we find the Bayesian evidence to be consistent between NS and NeuTra–NS runs. These values are shown in Appendix F and are also close to the mean of the ELBO from the last 100 epochs of NeuTra training, -10.04 .

Lastly, our result represents the first NSI parameter space scan for direct detection experiments whereby all the parameters are allowed to vary simultaneously. A similar scan was carried out

in [9]; however, only two parameters were allowed to vary at once. Our approach instead captures the full complexity of this space, allowing us to draw full multi-dimensional credible regions.

4 Conclusions

We have achieved significant performance improvements in Bayesian inference compared to techniques traditional to the astroparticle physics community. We accomplished this by leveraging GPU acceleration, automatic differentiation, and neural-network-guided reparameterization, benchmarking their performances against nested sampling alone. As our physics application, we have made inferences in the multi-dimensional parameter space of neutrino non-standard interactions using the astroparticle experiments XENON1T and PandaX-4T. We have achieved a factor ~ 100 performance boost compared to nested sampling alone without compromising the accuracy of the results, also producing the first parameter space scan for direct detection experiments where all NSI parameters are allowed to vary simultaneously.

We began by using a multivariate Gaussian model to evaluate the performances of nested sampling and the No U-Turn Sampler (NUTS), both with and without neural transport. We found that neural transport improved their performances by factors of ~ 2 and ~ 9 , respectively. For this synthetic problem, NUTS was more performant at posterior distribution sampling than nested sampling.

Applying these methods to our astroparticle physics scenario, we found that GPUs accelerated likelihood evaluations by a factor of ~ 20 and that NUTS was faster than nested sampling by a factor of ~ 2 . Finally, reparameterization using neural transport, whereby our posteriors were first mapped to Gaussian geometries, gave us a total factor of ~ 60 improvement with NUTS and ~ 100 with nested sampling compared to nested sampling on the CPU without neural transport. Unlike in the Gaussian fit, the performance of NUTS was lower than that of nested sampling when neural transport was employed, demonstrating that the optimal method depends on the specific problem at hand. In addition, since nested sampling allows for the computation of the Bayesian evidence, this work represents a way to accelerate model comparison while retaining compatibility with existing nested sampling implementations that are widely used in the natural sciences.

Our results underscore the potential of advanced computational techniques to transform inference and model comparison in astroparticle physics. The performance improvements we have achieved will aid in diagnosing convergence issues, incorporating additional experimental data, and producing new research. Moreover, these methods can be extended to other areas featuring multi-dimensional parameter spaces.

4.1 Limitations and Future Work

For our neutrino physics experiments, the computational resource used to train the neural transport model was insignificant compared to the sampling process. This may not be true if only a small posterior sample is needed, and thus whether neural transport would yield performance improvements would depend on the desired posterior sample size. We note that the effectiveness of neural transport is dependent on the ability of the trained normalizing flow to represent the desired posterior distribution [69] and that Neural transport requires manual tuning for individual problems. For future work, we will assess how comparing the Bayesian evidence evaluated using nested sampling and the ELBO from neural transport training can be used as a diagnostic for both the convergence of nested sampling and the training of the normalizing flow.

Finally, we are applying the methods in this work to so-called *global fits* of neutrino properties. In these fits, multi-dimensional parameter spaces are independently scanned for multiple experiments, and they are produced by collaborations such as NuFIT [70]. Combining the constraining power from many experiments—especially those with multiple measurement channels such as DUNE [71], PandaX [72], and XENONnT [73]—will make our methods particularly pertinent. This is because each experiment will have an associated complex posterior geometry to traverse that can benefit from the techniques we have explored.

Acknowledgments and Disclosure of Funding

We thank Aarón Higuera for insightful discussions throughout this work. We also thank Fangda Gu, Ray Hagimoto, Aarón Higuera, Ivy Li, and Andre Scaffidi for their comments on the manuscript. This work is supported by the Department of Energy AI for HEP program, Rice University, and The National Science Foundation award PHY-204659. We thank Nvidia for supplying us with the Titan V GPUs used in this work.

References

- [1] Hitoshi Murayama. Physics Beyond the Standard Model and Dark Matter. In *Les Houches Summer School - Session 86: Particle Physics and Cosmology: The Fabric of Spacetime*, 4 2007.
- [2] B. C. Allanach. Beyond the Standard Model Lectures for the 2016 European School of High-Energy Physics. In *2016 European School of High-Energy Physics*, pages 123–152, 2017.
- [3] Hyun Min Lee. Lectures on physics beyond the Standard Model. *J. Korean Phys. Soc.*, 78(11):985–1017, 2021.
- [4] JiJi Fan, Matthew Reece, and Lian-Tao Wang. Non-relativistic effective theory of dark matter direct detection. *JCAP*, 11:042, 2010.
- [5] Farhan Feroz, Kyle Cranmer, Mike Hobson, Roberto Ruiz de Austri, and Roberto Trotta. Challenges of Profile Likelihood Evaluation in Multi-Dimensional SUSY Scans. *JHEP*, 06:042, 2011.
- [6] Michèle Levi. Effective Field Theories of Post-Newtonian Gravity: A comprehensive review. *Rept. Prog. Phys.*, 83(7):075901, 2020.
- [7] Carlos A. Argüelles, Nicolò Foppiani, and Matheus Hostert. Efficiently exploring multidimensional parameter spaces beyond the Standard Model. *Phys. Rev. D*, 107(3):035027, 2023.
- [8] Gino Isidori, Felix Wilsch, and Daniel Wyler. The standard model effective field theory at work. *Rev. Mod. Phys.*, 96(1):015006, 2024.
- [9] Dorian W. P. Amaral, David Cerdeno, Andrew Cheek, and Patrick Foldenauer. A direct detection view of the neutrino NSI landscape. *JHEP*, 07:071, 2023.
- [10] Xi Chen, Mike Hobson, Saptarshi Das, and Paul Gelderblom. Improving the efficiency and robustness of nested sampling using posterior repartitioning. *arXiv e-prints*, page arXiv:1803.06387, March 2018.
- [11] D. G. Cerdeño, A. Cheek, E. Reid, and H. Schulz. Surrogate Models for Direct Dark Matter Detection. *JCAP*, 08:011, 2018.
- [12] Joshua G. Albert. JAXNS: a high-performance nested sampling package based on JAX. *arXiv e-prints*, page arXiv:2012.15286, December 2020.
- [13] Roberto Trotta, Roberto Trotta, Farhan Feroz, Michael P. Hobson, Leszek Roszkowski, and R. Ruiz de Austri. The impact of priors and observables on parameter inferences in the constrained mssm. *Journal of High Energy Physics*, 2008:024–024, 2008.
- [14] James Bradbury, Roy Frostig, Peter Hawkins, Matthew James Johnson, Chris Leary, Dougal Maclaurin, George Necula, Adam Paszke, Jake VanderPlas, Skye Wanderman-Milne, and Qiao Zhang. JAX: composable transformations of Python+NumPy programs, 2018.
- [15] Eli Bingham, Jonathan P. Chen, Martin Jankowiak, Fritz Obermeyer, Neeraj Pradhan, Theofanis Karaletsos, Rohit Singh, Paul Szerlip, Paul Horsfall, and Noah D. Goodman. Pyro: Deep Universal Probabilistic Programming. *Journal of Machine Learning Research*, 2018.

- [16] Du Phan, Neeraj Pradhan, and Martin Jankowiak. Composable effects for flexible and accelerated probabilistic programming in numpyro. *arXiv preprint arXiv:1912.11554*, 2019.
- [17] S. Duane, A. D. Kennedy, B. J. Pendleton, and D. Roweth. Hybrid Monte Carlo. *Phys. Lett. B*, 195:216–222, 1987.
- [18] Radford M. Neal. Mcmc using hamiltonian dynamics. *arXiv: Computation*, pages 139–188, 2011.
- [19] Matthew D Hoffman, Andrew Gelman, et al. The no-u-turn sampler: adaptively setting path lengths in hamiltonian monte carlo. *J. Mach. Learn. Res.*, 15(1):1593–1623, 2014.
- [20] Matthew Hoffman, Pavel Sountsov, Joshua V. Dillon, Ian Langmore, Dustin Tran, and Srinivas Vasudevan. NeuTra-lizing Bad Geometry in Hamiltonian Monte Carlo Using Neural Transport. *arXiv e-prints*, page arXiv:1903.03704, March 2019.
- [21] L. Wolfenstein. Neutrino Oscillations in Matter. *Phys. Rev. D*, 17:2369–2374, 1978.
- [22] M. M. Guzzo, A. Masiero, and S. T. Petcov. On the MSW effect with massless neutrinos and no mixing in the vacuum. *Phys. Lett. B*, 260:154–160, 1991.
- [23] M. M. Guzzo and S. T. Petcov. On the matter-enhanced transitions of solar neutrinos in the absence of neutrino mixing in vacuum. *Phys. Lett. B*, 271:172–178, 1991.
- [24] M. C. Gonzalez-Garcia, M. M. Guzzo, P. I. Krastev, H. Nunokawa, O. L. G. Peres, V. Pleitez, J. W. F. Valle, and R. Zukanovich Funchal. Atmospheric neutrino observations and flavor changing interactions. *Phys. Rev. Lett.*, 82:3202–3205, 1999.
- [25] M. M. Guzzo, H. Nunokawa, P. C. de Holanda, and O. L. G. Peres. On the massless 'just-so' solution to the solar neutrino problem. *Phys. Rev. D*, 64:097301, 2001.
- [26] M. Guzzo, P. C. de Holanda, M. Maltoni, H. Nunokawa, M. A. Tortola, and J. W. F. Valle. Status of a hybrid three neutrino interpretation of neutrino data. *Nucl. Phys. B*, 629:479–490, 2002.
- [27] M. C. Gonzalez-Garcia and Michele Maltoni. Atmospheric neutrino oscillations and new physics. *Phys. Rev. D*, 70:033010, 2004.
- [28] Ivan Esteban, M. C. Gonzalez-Garcia, Michele Maltoni, Ivan Martinez-Soler, and Jordi Salvado. Updated constraints on non-standard interactions from global analysis of oscillation data. *JHEP*, 08:180, 2018. [Addendum: *JHEP* 12, 152 (2020)].
- [29] E. Aprile et al. Search for Coherent Elastic Scattering of Solar ^8B Neutrinos in the XENON1T Dark Matter Experiment. *Phys. Rev. Lett.*, 126:091301, 2021.
- [30] Xiaoying Lu et al. A Measurement of Solar pp Neutrino Flux using PandaX-4T Electron Recoil Data. *arXiv preprint arXiv:2401.07045*, 1 2024.
- [31] John Skilling. Nested Sampling. *AIP Conference Proceedings*, 735(1):395–405, 11 2004.
- [32] Johannes Buchner. Nested sampling methods. *Statistics Surveys*, 17:169 – 215, 2023.
- [33] John Skilling. Nested sampling for general Bayesian computation. *Bayesian Analysis*, 1(4):833 – 859, 2006.
- [34] Patricio Maturana Russel, Brendon J Brewer, Steffen Klaere, and Remco R Bouckaert. Model selection and parameter inference in phylogenetics using nested sampling. *Systematic biology*, 68(2):219–233, 2019.
- [35] Shreyas Arvindkar, Aditi S Pathak, Kartik Majila, and Shruthi Viswanath. Optimizing representations for integrative structural modeling using bayesian model selection. *Bioinformatics*, 40(3):btac106, 2024.

- [36] Laurent Sagart, Guillaume Jacques, Yunfan Lai, Robin J Ryder, Valentin Thouzeau, Simon J Greenhill, and Johann-Mattis List. Dated language phylogenies shed light on the ancestry of sino-tibetan. *Proceedings of the National Academy of Sciences*, 116(21):10317–10322, 2019.
- [37] Martine Robbeets and Remco Bouckaert. Bayesian phylolinguistics reveals the internal structure of the transeurasian family. *Journal of Language Evolution*, 3(2):145–162, 2018.
- [38] Greg Ashton et al. Nested sampling for physical scientists. *Nature Reviews Methods Primers*, 2(1):39, 2022.
- [39] David Yallup, Timo Janßen, Steffen Schumann, and Will Handley. Exploring phase space with Nested Sampling. *Eur. Phys. J. C*, 82:8, 2022.
- [40] Bhaskar Dutta, Rafael F. Lang, Shu Liao, Samiran Sinha, Louis Strigari, and Adrian Thompson. A global analysis strategy to resolve neutrino NSI degeneracies with scattering and oscillation data. *JHEP*, 09:106, 2020.
- [41] Michael Betancourt. A Conceptual Introduction to Hamiltonian Monte Carlo. 1 2017.
- [42] Matthew Hoffman, Alexey Radul, and Pavel Sountsov. An adaptive-mcmc scheme for setting trajectory lengths in hamiltonian monte carlo. In *Proceedings of The 24th International Conference on Artificial Intelligence and Statistics*, volume 130 of *Proceedings of Machine Learning Research*, pages 3907–3915. PMLR, 13–15 Apr 2021.
- [43] Matthew D. Hoffman and Pavel Sountsov. Tuning-free generalized hamiltonian monte carlo. In *Proceedings of The 25th International Conference on Artificial Intelligence and Statistics*, volume 151 of *Proceedings of Machine Learning Research*, pages 7799–7813. PMLR, 28–30 Mar 2022.
- [44] Bob Carpenter, Andrew Gelman, Matthew D Hoffman, Daniel Lee, Ben Goodrich, Michael Betancourt, Marcus A Brubaker, Jiqiang Guo, Peter Li, and Allen Riddell. Stan: A probabilistic programming language. *Journal of statistical software*, 76, 2017.
- [45] Abril-Pla Oriol, Andreani Virgile, Carroll Colin, Dong Larry, Fonnesbeck Christopher J., Kochurov Maxim, Kumar Ravin, Lao Jupeng, Luhmann Christian C., Martin Osvaldo A., Osthege Michael, Vieira Ricardo, Wiecki Thomas, and Zinkov Robert. Pymc: A modern and comprehensive probabilistic programming framework in python. *PeerJ Computer Science*, 9:e1516, 2023.
- [46] Wendy L. Freedman. Measurements of the Hubble Constant: Tensions in Perspective. *Astrophys. J.*, 919(1):16, 2021.
- [47] Mrinank Sharma, Sören Mindermann, Charlie Rogers-Smith, Gavin Leech, Benedict Snodin, Janvi Ahuja, Jonas B Sandbrink, Joshua Teperowski Monrad, George Altman, Gurpreet Dhaliwal, et al. Understanding the effectiveness of government interventions against the resurgence of covid-19 in europe. *Nature communications*, 12(1):5820, 2021.
- [48] Chaoming Wang, Xiaoyu Chen, Tianqiu Zhang, and Si Wu. Brainpy: a flexible, integrative, efficient, and extensible framework towards general-purpose brain dynamics programming. *bioRxiv*, 2022.
- [49] Luna Fazio and Paul-Christian Burkner. Gaussian distributional structural equation models: A framework for modeling latent heteroscedasticity. 2024.
- [50] MA Acero, B Acharya, P Adamson, N Anfimov, A Antoshkin, E Arrieta-Diaz, L Asquith, A Aurisano, A Back, N Balashov, et al. Expanding neutrino oscillation parameter measurements in nova using a bayesian approach. *arXiv preprint arXiv:2311.07835*, 2023.
- [51] Jean-Eric Campagne, François Lanusse, Joe Zuntz, Alexandre Boucaud, Santiago Casas, Minas Karamanis, David Kirkby, Denise Lanzieri, Yin Li, and Austin Peel. JAX-COSMO: An End-to-End Differentiable and GPU Accelerated Cosmology Library. *Open J. Astrophys.*, 6:1–15, 2023.

- [52] J. Ruiz-Zapatero, D. Alonso, C. García-García, A. Nicola, A. Mootoovaloo, J. M. Sullivan, M. Bonici, and P. G. Ferreira. LimberJack.jl: auto-differentiable methods for angular power spectra analyses. 10 2023.
- [53] Omiros Papaspiliopoulos, Gareth O. Roberts, and Martin Skold. A general framework for the parametrization of hierarchical models. *Statistical Science*, 22:59–73, 2007.
- [54] Maria Gorinova, Dave Moore, and Matthew Hoffman. Automatic reparameterisation of probabilistic programs. In Hal Daumé III and Aarti Singh, editors, *Proceedings of the 37th International Conference on Machine Learning*, volume 119 of *Proceedings of Machine Learning Research*, pages 3648–3657. PMLR, 13–18 Jul 2020.
- [55] Nicola De Cao, Wilker Aziz, and Ivan Titov. Block neural autoregressive flow. In Ryan P. Adams and Vibhav Gogate, editors, *Proceedings of The 35th Uncertainty in Artificial Intelligence Conference*, volume 115 of *Proceedings of Machine Learning Research*, pages 1263–1273. PMLR, 22–25 Jul 2020.
- [56] Rajesh Ranganath, Sean Gerrish, and David M. Blei. Black box variational inference. In *International Conference on Artificial Intelligence and Statistics*, 2013.
- [57] Diederik P Kingma and Max Welling. Auto-encoding variational bayes. *arXiv preprint arXiv:1312.6114*, 2013.
- [58] Raymond Davis, Jr., Don S. Harmer, and Kenneth C. Hoffman. Search for neutrinos from the sun. *Phys. Rev. Lett.*, 20:1205–1209, 1968.
- [59] Q. R. Ahmad et al. Measurement of the rate of $\nu_e + d \rightarrow p + p + e^-$ interactions produced by ^8B solar neutrinos at the Sudbury Neutrino Observatory. *Phys. Rev. Lett.*, 87:071301, 2001.
- [60] Mohammad Sajjad Athar et al. Status and perspectives of neutrino physics. *Prog. Part. Nucl. Phys.*, 124:103947, 2022.
- [61] J. Aalbers et al. A next-generation liquid xenon observatory for dark matter and neutrino physics. *J. Phys. G*, 50(1):013001, 2023.
- [62] E. Aprile et al. The XENON1T Dark Matter Experiment. *Eur. Phys. J. C*, 77(12):881, 2017.
- [63] Hongguang Zhang et al. Dark matter direct search sensitivity of the PandaX-4T experiment. *Sci. China Phys. Mech. Astron.*, 62(3):31011, 2019.
- [64] Dorian W. P. Amaral, David G. Cerdeño, Andrew Cheek, and Patrick Foldenauer. SNUDD [Computer Software], available at <https://github.com/snudd/snudd.git>, 2023.
- [65] Radford M Neal. Slice sampling. *The annals of statistics*, 31(3):705–767, 2003.
- [66] Johannes Buchner. UltraNest - a robust, general purpose Bayesian inference engine. *The Journal of Open Source Software*, 6(60):3001, April 2021.
- [67] Pablo Gómez, Håvard Hem Toftevaag, and Gabriele Meoni. torchquad: Numerical Integration in Arbitrary Dimensions with PyTorch. *Journal of Open Source Software*, 64(6), 2021.
- [68] Daniel Foreman-Mackey. corner.py: Scatterplot matrices in python. *The Journal of Open Source Software*, 1(2):24, jun 2016.
- [69] Louis Grenioux, Alain Oliviero Durmus, Eric Moulines, and Marylou Gabrié. On sampling with approximate transport maps. In *Proceedings of the 40th International Conference on Machine Learning*, volume 202 of *Proceedings of Machine Learning Research*, pages 11698–11733. PMLR, 2023.
- [70] Ivan Esteban, M. C. Gonzalez-Garcia, Michele Maltoni, Thomas Schwetz, and Albert Zhou. The fate of hints: updated global analysis of three-flavor neutrino oscillations. *JHEP*, 09:178, 2020.

- [71] Babak Abi et al. Deep Underground Neutrino Experiment (DUNE), Far Detector Technical Design Report, Volume II: DUNE Physics. 2 2020.
- [72] XiGuang Cao et al. PandaX: A Liquid Xenon Dark Matter Experiment at CJPL. *Sci. China Phys. Mech. Astron.*, 57:1476–1494, 2014.
- [73] E. Aprile et al. The XENONnT Dark Matter Experiment. 2 2024.
- [74] Aki Vehtari, Andrew Gelman, Daniel P. Simpson, Bob Carpenter, and Paul-Christian Burkner. Rank-normalization, folding, and localization: An improved \hat{r} for assessing convergence of mcmc (with discussion). *Bayesian Analysis*, 2019.
- [75] Ravin Kumar, Colin Carroll, Ari Hartikainen, and Osvaldo Martin. Arviz a unified library for exploratory analysis of bayesian models in python. *Journal of Open Source Software*, 4(33):1143, 2019.
- [76] Leslie Kish. *Survey sampling*. J. Wiley, New York, 1965.

A Reparameterizing Probability Density Functions

Let $\mathbf{f} : \mathbb{R}^n \rightarrow \mathbb{R}^n$ denote an arbitrary coordinate transformation onto the same space. This function takes the vector of random variables $\mathbf{X} \equiv (X_1, X_2, \dots, X_n)^\top$ and maps it onto the transformed random variable vector $\mathbf{Y} \equiv \mathbf{f}(\mathbf{X}) \equiv (Y_1, Y_2, \dots, Y_n)^\top$. The change in the volume element from the first basis to the second is characterized by the determinant of the Jacobian

$$\frac{\partial \mathbf{f}}{\partial \mathbf{x}} \equiv \begin{pmatrix} \frac{\partial f_1}{\partial x_1} & \cdots & \frac{\partial f_1}{\partial x_n} \\ \vdots & \ddots & \vdots \\ \frac{\partial f_n}{\partial x_1} & \cdots & \frac{\partial f_n}{\partial x_n} \end{pmatrix}. \quad (9)$$

Consider the joint-probability density of the transformed and original variables, respectively $\rho_Y(\mathbf{y})$ and $\rho_X(\mathbf{x})$. Since probabilities within equal volumes must remain fixed, we have that

$$\int_{\mathbf{f}(\Omega)} \rho_Y(\mathbf{y}) d^n \mathbf{y} = \int_{\Omega} \rho_X[\mathbf{f}(\mathbf{x})] \left| \frac{\partial \mathbf{f}}{\partial \mathbf{x}} \right| d^n \mathbf{x}, \quad (10)$$

where Ω is the integration domain with respect to the original variables. We can thus identify the probability density

$$\rho_X(\mathbf{x}) = \rho_Y[\mathbf{f}(\mathbf{x})] \left| \frac{\partial \mathbf{f}}{\partial \mathbf{x}} \right|, \quad (11)$$

which is the form of Eq. (3). Note that a similar procedure can be used to relate $\rho_Y(\mathbf{y})$ to $\rho_X(\mathbf{x})$ via

$$\rho_Y(\mathbf{y}) = \rho_X[\mathbf{f}^{-1}(\mathbf{y})] \left| \frac{\partial \mathbf{x}}{\partial \mathbf{f}} \right|, \quad (12)$$

where $|\partial \mathbf{x} / \partial \mathbf{f}|$ is the determinant of the inverse of the Jacobian given in Eq. (9).

B Neutrino Non-Standard Interactions

Neutrino non-standard interactions (NSI) is a physics framework describing potential novel phenomena that can occur with fundamental particles known as neutrinos. We can model these phenomena via the parameterization described in Section 2.2 and visualized in Fig. 1. The physics underlying neutrino NSI can also be represented as per Fig. 4, where a neutrino of flavor α interacts with a particle (proton, neutron, or electron) and leaves as a neutrino of flavor β . The strength of this interaction is captured by the parameter $\varepsilon_{\alpha\beta}$, and how much of it takes place with these three particles is described by the angles η and φ .

Concretely, the interactions with these particles can be written via the transformation equations

$$\varepsilon_{\alpha\beta}^p = \sqrt{5} \varepsilon_{\alpha\beta} \cos \eta \cos \varphi, \quad \varepsilon_{\alpha\beta}^e = \sqrt{5} \varepsilon_{\alpha\beta} \cos \eta \sin \varphi, \quad \varepsilon_{\alpha\beta}^n = \sqrt{5} \varepsilon_{\alpha\beta} \sin \eta, \quad (13)$$

where the factor of $5^{1/2}$ is a convention in the field [9, 28]. Except for this factor, this system of equations can be seen to be the projection from the ‘spherical’ NSI parameterization onto a ‘Cartesian’ one. Ultimately, the predictions made by the SNUDD codebase are based on the values of these latter parameters [9, 64].

We rely on the physical intuition behind these variables when considering the priors to place on the parameters $(\varepsilon_{\alpha\beta}, \eta, \varphi)$, described in Section 3.2 and given explicitly in Eq. (8). Firstly, we expect that the intrinsic strength of the new neutrino interaction for any flavor combination, captured by $\varepsilon_{\alpha\beta}$, should not have any preferred value. Hence, it should be uniformly distributed over a wide range. Secondly, given a value for this interaction strength, we do not expect any preference for the specific particle with which the neutrino interacts. Thus, we posit that the surface of the sphere in the spherical NSI space defined by the fixed radius $\varepsilon_{\alpha\beta}$ should be evenly sampled. To achieve this, we can inspect Eq. (13) to notice that these transformations are nothing but the usual spherical–Cartesian transformations with the polar angle θ replaced by the latitude angle $\eta \equiv \pi/2 - \theta$. In spherical polars, we evenly populate the surface of a sphere by sampling $\cos \theta \sim \text{Uniform}(-1, 1)$; in our case, it thus suffices to make the replacement $\cos \theta \rightarrow \sin \eta$. Lastly, the polar angle φ is uniformly sampled in the range $(-\pi/2, \pi/2)$ instead of the usual $(0, 2\pi)$ because the ‘radius’ of the sphere, given by $\varepsilon_{\alpha\beta}$, is allowed to take on negative values.

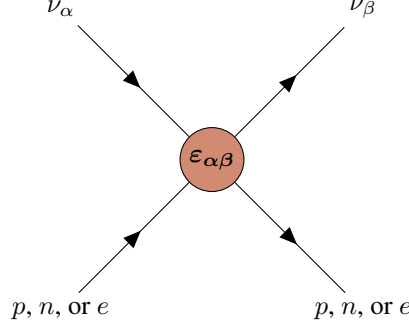


Figure 4: The neutrino non-standard interactions (NSI) picture. A neutrino (ν) of flavor α interacts with a proton (p), a neutron (n), or an electron (e) and leaves as a neutrino of flavor β . The strength of this new interaction is parameterized by the variable $\varepsilon_{\alpha\beta}$.

C Ground Truth Bayesian Evidence and Contour for Synthetic Model

We consider a generalized version of the synthetic model we introduced in Section 3.1, with parameters $\boldsymbol{\theta} \in \mathbb{R}^k$ and data matrix $\mathbf{X} \in \mathbb{R}^{k \times n}$, such that $\mathbf{X} \equiv (\mathbf{x}_1, \mathbf{x}_2, \dots, \mathbf{x}_n)^\top$ with $\mathbf{x}_i \in \mathbb{R}^k$. Each random vector \mathbf{x}_i represents a vector of random variables sampled from a k -dimensional Gaussian. The likelihood is then given by

$$\ell(\boldsymbol{\theta}; \mathbf{X}) = \prod_{i=1}^k \prod_{j=1}^n \frac{1}{\sqrt{2\pi\sigma_i^2}} \exp \left[-\frac{1}{2} \left(\frac{X_{ij} - \mu_i}{\sigma_i^2} \right)^2 \right]. \quad (14)$$

As σ_i^2 needs to be strictly positive, we instead define priors on $\mathcal{C}_i = \log \sigma_i^2$. Our parameters are then $\boldsymbol{\theta} \equiv (\mu_1, \dots, \mu_{k/2}, \mathcal{C}_1, \dots, \mathcal{C}_{k/2})^\top$. We use the same model as Eq. (7), such that our prior distribution is given by

$$\pi(\boldsymbol{\theta}) = \prod_{i=1}^k \frac{1}{\sqrt{2\pi\tilde{\sigma}^2}} \exp \left[-\frac{\mu_i^2}{2\tilde{\sigma}^2} \right] \exp \left[-\frac{\mathcal{C}_i^2}{2\tilde{\sigma}^2} \right], \quad (15)$$

where the variance for all parameters is set to $\tilde{\sigma}^2 = 10$.

We first wish to calculate the Bayesian evidence integral, given by

$$\mathcal{Z} \equiv \int \ell(\boldsymbol{\theta}; \mathbf{X}) \pi(\boldsymbol{\theta}) d^k \boldsymbol{\theta}. \quad (16)$$

To reduce computational cost, we perform the integrals over $\boldsymbol{\mu}$ analytically. This halves the number of integrals that need to be done numerically and improves the performance scaling from $O(N^{2k})$ to $O(N^k)$, given N integration sample points per dimension.

We may write Eq. (16) as

$$\mathcal{Z} = \frac{1}{(2\pi)^{nk/2}} \frac{1}{(2\pi\tilde{\sigma}^2)^k} \prod_{i=1}^k \iint e^{-n\mathcal{C}_i} e^{-\mathcal{E}_i(\mu_i)} d^{k/2} \boldsymbol{\mu} d^{k/2} \mathcal{C}, \quad (17)$$

where the exponent \mathcal{E}_i has been defined to be

$$\mathcal{E}_i(\mu_i) \equiv a_i \mu_i^2 + b_i \mu_i + c_i, \quad (18)$$

with

$$a_i \equiv \frac{1}{2} \left(\frac{1}{\tilde{\sigma}^2} + n e^{-2\mathcal{C}_i} \right), \quad b_i \equiv -e^{-2\mathcal{C}_i} \sum_{j=1}^n y_{ij}, \quad c_i \equiv \frac{1}{2} \left(\frac{\mathcal{C}_i^2}{\tilde{\sigma}^2} + e^{-2\mathcal{C}_i} \sum_{j=1}^n y_{ij}^2 \right). \quad (19)$$

Integrating over any one particular μ_i then gives us

$$\int_{-\infty}^{\infty} e^{-\mathcal{E}_i(\mu_i)} d\mu_i \equiv \mathcal{I}_i \equiv \sqrt{\frac{\pi}{a_i}} \exp \left(\frac{b_i^2 - 4a_i c_i}{4a_i} \right), \quad (20)$$

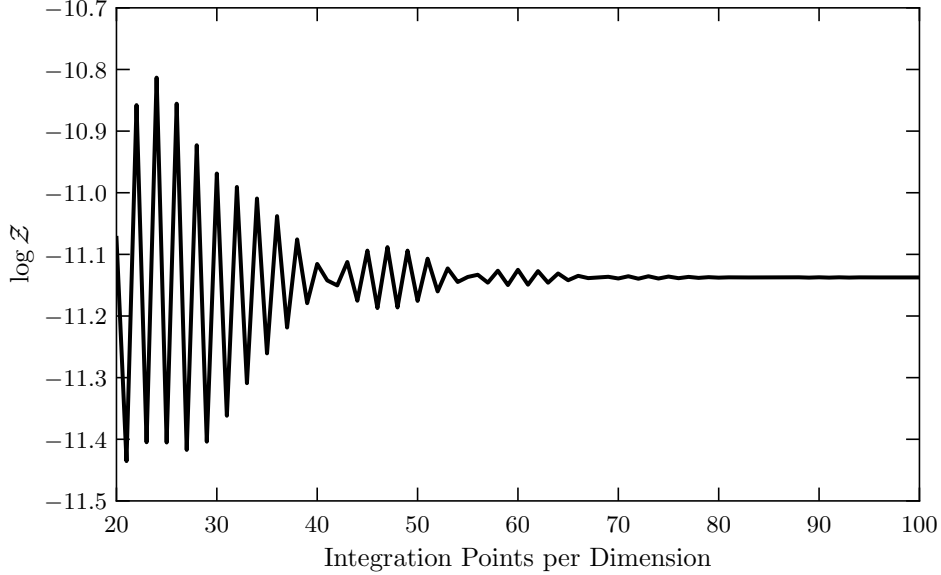


Figure 5: Log of Bayesian evidence integral $\log \mathcal{Z}$ for synthetic model, Eq. (16), with number of integration points per parameter dimension. For this model, the number of dimensions is $k = 3$ and the number of data points is $j = 2$. The integral converges to the quoted value of $\log \mathcal{Z} \approx -11.14$ after approximately 60 points.

such that

$$\mathcal{Z} = \frac{1}{(2\pi)^{nk/2}} \frac{1}{(2\pi\tilde{\sigma}^2)^k} \prod_{i=1}^k \int e^{-nC_i \mathcal{I}_i} d^{k/2} \mathcal{C}. \quad (21)$$

The remaining $k/2$ integrals on \mathcal{C}_i can be done numerically.

For the numerical integration, we use the `torchquad` package [67]. In the particular synthetic model described in Section 3.1, we have $k = 3$ dimensions and $j = 2$ data points. We use the trapezoid procedure with a domain of $[-50, 50]$ for both μ_i and \mathcal{C}_i , and we use 151 integration points per dimension. The domain was chosen to be far from the contours; this was verified by increasing the integration domain to $[80, 80]$, scaling the integration points per dimension to 241, and checking that the value of the integral does not appreciably change. We ensure the integral has converged by verifying that $\log \mathcal{Z}$ does not change when the number of integration points per dimension is increased, as shown in Fig. 5. We converge to the quoted value of $\log \mathcal{Z} \approx -11.14$ after approximately 60 points, and subsequently conservatively choose 151 points for numerical integrals used in this paper. This corresponds to 151^3 points for the $\log \mathcal{Z}$ integral, and 151^2 points for the μ_1 versus \mathcal{C}_1 contour.

To compute the ground truth contour, the two variables on which the contour is projected are excluded from the integral in Eq. (16), producing the quantity

$$\mathcal{F}(\theta_u, \theta_v) \equiv \int \ell(\theta_u, \theta_v, \boldsymbol{\theta}'; \mathbf{X}) \pi(\theta_u, \theta_v, \boldsymbol{\theta}') d^{k-2} \boldsymbol{\theta}', \quad (22)$$

where θ_u and θ_v are the variables that are used to produce the contour, and $\boldsymbol{\theta}'$ is the set of variables excluding θ_u and θ_v . $\mathcal{F}(\theta_u, \theta_v)$ is then computed using the same procedure described above for each set of θ_u and θ_v . A $\rho\%$ contour level can be described by the equation $\varsigma_{\rho\%} = \mathcal{F}(\theta_u, \theta_v)$, where

$$\frac{\int \mathcal{F}'(\theta_u, \theta_v) d\theta_u d\theta_v}{\int \mathcal{F}(\theta_u, \theta_v) d\theta_u d\theta_v} = \rho\%, \quad \text{with} \quad \mathcal{F}'(\theta_u, \theta_v) \equiv \begin{cases} \mathcal{F}(\theta_u, \theta_v) & \text{if } \mathcal{F}(\theta_u, \theta_v) > \varsigma_{\rho\%} \\ 0 & \text{if } \mathcal{F}(\theta_u, \theta_v) \leq \varsigma_{\rho\%} \end{cases}. \quad (23)$$

We show the ground truth μ_1 - \mathcal{C}_1 contour in Fig. 2.

D Effective Sample Size Calculation

The effective sample size (ESS) for MCMC chains, as implemented in ArviZ, is given by [74, 75]

$$N_{\text{eff}} = \frac{MN}{\tau}, \quad \tau = -1 + 2 \sum_{t=0}^K P_{t'}, \quad \text{and} \quad P_{t'} = \rho_{2t'} + \rho_{2t'+1}, \quad (24)$$

where M is the number of chains, N is the number of samples per chain, ρ_t is the estimated auto-correlation at time t , and K is the largest integer for which $P_K = \rho_{2K} + \rho_{2K+1}$ remains positive. As nested sampling produces weighted samples, the effective sample size is instead computed using Kish's design effect [76], as implemented in `ultranest` [66]:

$$D_{\text{eff}} = 1 + \frac{1}{N} \sum_{i=1}^N (Nw_i - 1)^2 \quad \text{and} \quad N_{\text{eff}} = \frac{N}{D_{\text{eff}}}, \quad (25)$$

where w_i are normalized weights that sum to 1 and N is the total number of weighted samples.

E Full Corner Plots

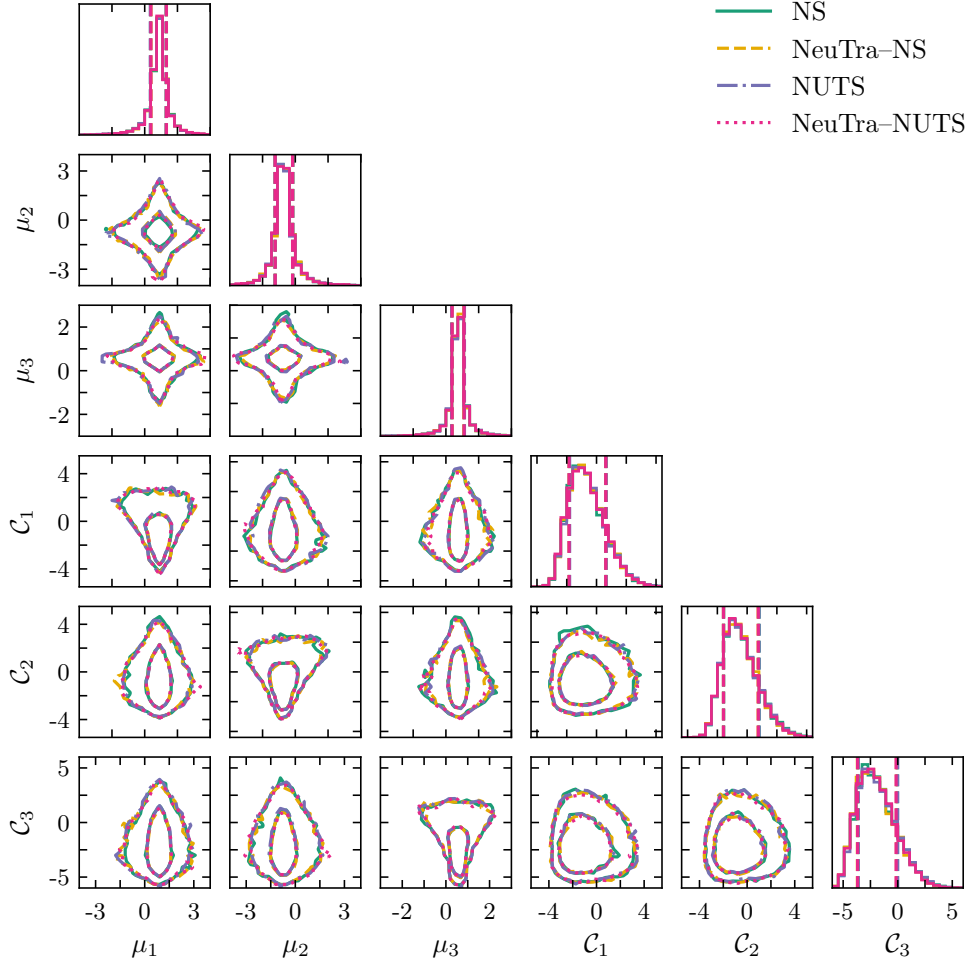


Figure 6: The same as in Fig. 2 but for the full synthetic model parameter space.

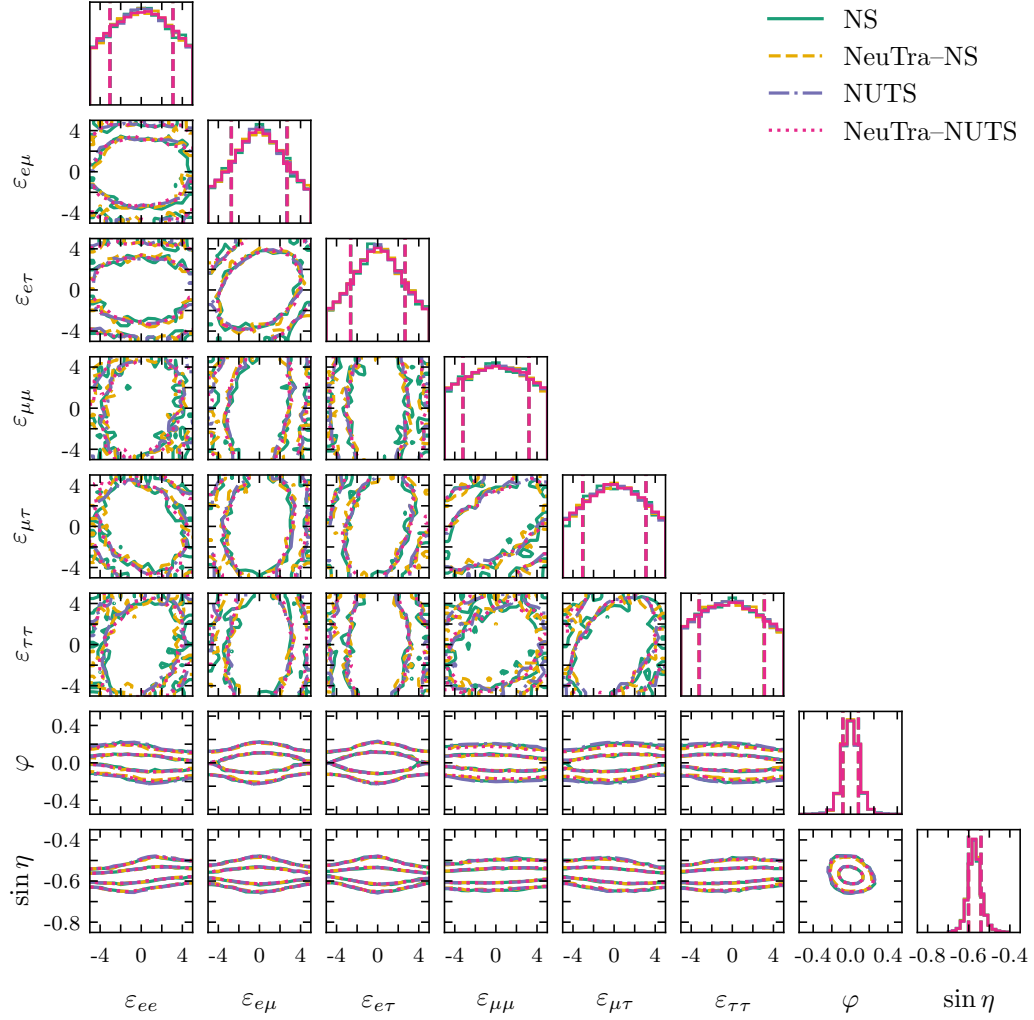


Figure 7: The same as in Fig. 3 but for the full NSI parameter space.

F Bayesian Evidence from Nested Sampling Runs

The Bayesian evidences from the Gaussian fit with unknown mean and variance and the neutrino physics model are shown in Table 3 and Table 4, respectively.

Run number	$\log \mathcal{Z}$ (NS)	$\log \mathcal{Z}$ (NeuTra-NS)
0	-11.17 ± 0.07	-11.19 ± 0.1
1	-11.1 ± 0.1	-11.13 ± 0.06
2	-11.14 ± 0.08	-11.14 ± 0.07
3	-11.1 ± 0.2	-11.16 ± 0.06

Table 3: Log of Bayesian evidence integral for the Gaussian fit, $\log \mathcal{Z}$, computed using nested sampling (NS), with and without neural transport (NeuTra). We see that the evidence typically has a lower uncertainty in the NeuTra-NS runs. The values from all runs match both the ELBO from neural transport training, -11.21 , and the ground truth value, -11.14 .

Run number	$\log \mathcal{Z}$ (NS)	$\log \mathcal{Z}$ (NeuTra-NS)
0	-9.7 ± 0.1	-9.8 ± 0.1
1	-9.89 ± 0.08	-9.8 ± 0.2
2	-9.8 ± 0.1	-9.8 ± 0.2
3	-9.97 ± 0.08	-9.6 ± 0.2
4	-9.8 ± 0.1	-9.8 ± 0.1
5	-9.7 ± 0.08	-9.9 ± 0.1

Table 4: Log of Bayesian evidence integral for the neutrino physics problem, $\log \mathcal{Z}$, computed using nested sampling (NS), with and without neural transport (NeuTra). We see that the evidence typically has a lower uncertainty in the NeuTra-NS runs. The values from all runs match the ELBO from neural transport training, -10.04 .